Direct Probe of Interplay between Local Structure and Superconductivity in FeTe$_{0.55}$Se$_{0.45}$

Wenzhi Lin,[†,§] Qing Li,[†,§] Brian C. Sales,[‡] Stephen Jesse,[†] Athena S. Sefat,[‡] Sergei V. Kalinin,[†,*] and Minghu Pan[†,*]

[†]Center for Nanophase Materials Sciences and [‡]Materials Science and Technology Division, Oak Ridge National Laboratory, Oak Ridge, Tennessee 37831, United States. [§]These authors contributed equally to this work.

ABSTRACT The relationship between atomically defined structures and physical properties in functional materials remains a subject of constant interest. We explore the interplay between local crystallographic structure, composition, and local superconductive properties in iron chalcogenide superconductors. Direct structural analysis of scanning tunneling microscopy data allows local lattice distortions and structural defects across an FeTe$_{0.55}$Se$_{0.45}$ surface to be explored on a single unit-cell level. Concurrent superconducting

gap (SG) mapping reveals suppression of the SG at well-defined structural defects, identified as a local structural distortion. The strong structural distortion causes the vanishing of the superconducting state. This study provides insight into the origins of superconductivity in iron chalcogenides by providing an example of atomic-level studies of the structure—property relationship.
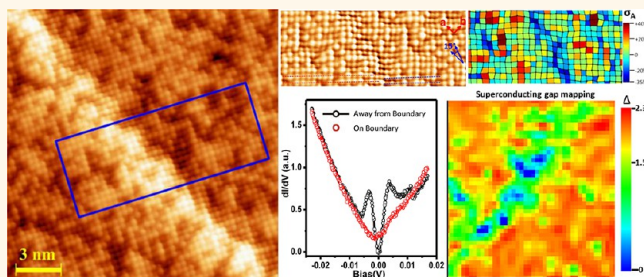
KEYWORDS: Fe-based superconductor · scanning tunneling microscopy · scanning tunneling spectroscopy

A key challenge in high-temperature superconductivity is to determine the role of local crystallographic structure and chemical effects on the superconducting critical temperature, T_c.[1−3] Iron chalcogenide superconductors (11) are ideal model systems for deciphering the role of local effects on the superconductivity, primarily because they cleave leaving nonpolar surfaces unlike other families of iron arsenide superconductors (1111 or 122) and cuprates.[4,5] There is no intervening ionic layer between the superconducting Fe(Se,Te) planes,[4] and so the cleaved surface is representative of the bulk crystal.[6] The layered nature of these materials makes them readily amenable to scanning tunneling microscopy (STM)-based studies. On the cleaved FeTe$_{0.55}$Se$_{0.45}$ surface, He *et al.*[7] identified the bright patches in STM images as tellurium atoms and the dark patches as selenium atoms. Hanaguri *et al.*[8] identified s± wave superconductivity on Fe(Se,Te). Song *et al.*[9] found a V-shaped gap on FeSe, suggesting strong evidence for nodal superconductivity.

Recently, emergence of mesoscopic scanning probe microscopy techniques has allowed exploring behaviors of functional materials on a single defect level. The examples include metallic domains in VO$_2$ by optical and microwave techniques,[10−14] piezoresponse force microscopy of polarization switching,[15−17] and many others. However, the atomic structure of these defects remains unknown.

To understand correlation between atomically resolved structure with crystallographic and chemical identities of atoms known and physical functionalities, we investigate FeTe$_{0.55}$Se$_{0.45}$ using STM and scanning tunneling spectroscopy (STS). Using a lab-built cryogenic STM, a structural distortion map across the FeTe$_{0.55}$Se$_{0.45}$ surface is derived from atomically resolved STM images. To quantify this behavior, we implement analysis of local crystallography from STM images using local bond-length analysis. Combination of these techniques allows for the identification of the local lattice distortion due to chemical inhomogeneity and defects. The electronic and superconductive properties are accessed from
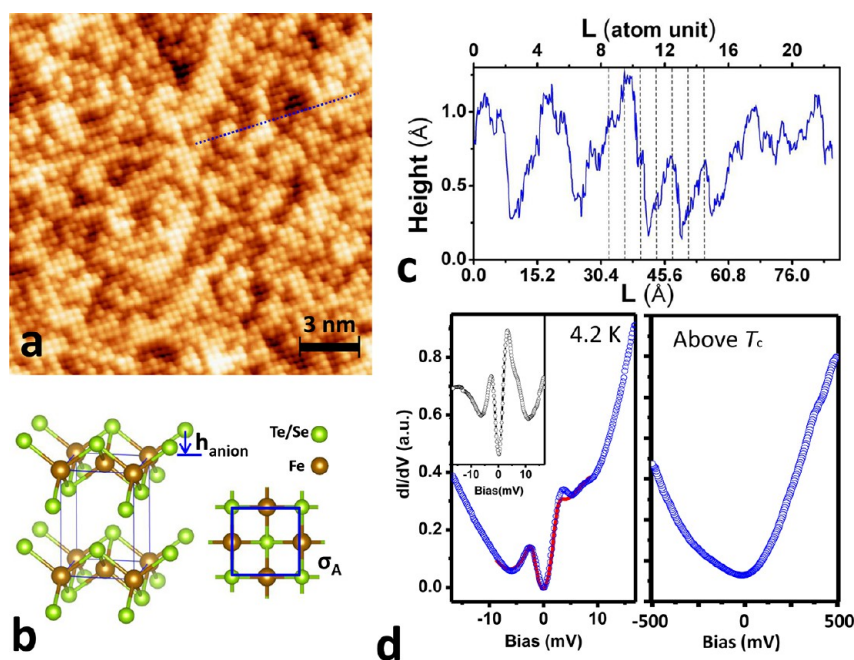
Figure 1. STM characterization of Fe(Se,Te). (a) Typical topographic image of the sample. The setup conditions for imaging were a sample bias voltage of 50 mV and a tunneling current of 0.1 nA. Atomically resolved image shows a lattice of chalcogens. **(b)** Model showing crystal structure, the anion height h_{anion}, and lattice area σ_A. **(c)** Line profile showing corrugation on the surface. The top horizontal axis is labeled with atom units (1 atom unit = 3.8 Å), and vertical dashed lines mark atomic positions in the line profile. **(d)** Averaged tunneling spectrum taken at about 4.2 and 77 K, both examined at the same surface. The solid red curve represents the fit of STS data to the Dynes function. Inset is the curve after the polynomial has been subtracted.

current-imaging tunneling spectroscopy (CITS) and differential conductance (dI/dV) measurements. Finally, superconducting gap (SG) mapping reveals suppression of SG at well-defined structural defects, which suggests a strong correlation between local structural distortion (symmetry-broken) and the suppression of superconducting states.

RESULTS AND DISCUSSION

Figure 1a presents a typical topographic STM image of the cleaved surface. The surface exhibits small patches of bright and dark contrast, in agreement with previous STM observations.[7] The surface corrugation between bright and dark patches is about 0.5 Å (Figure 1c), which is comparable with the results reported previously.[7] The corrugation is attributable to surface chemical clustering of Se/Te. Atomic resolution topographic image reveals a square lattice with a periodicity of approximately 3.8 Å, consistent with the in-plane lattice constant of the single crystal used in this study[18] and corresponding to the distance between adjacent apical chalcogen atoms of the Fe(Se,Te)$_4$ tetrahedra at the top of the cleaved surface. A spatially averaged tunneling spectrum taken at ~4.2 K is presented in the left panel of Figure 1d and shows an asymmetric V-shaped background at high energies and a gap in the low-energy regime, centered at the Fermi energy. Considering the fact that the gap vanishes at elevated temperature above T_c (right panel

of Figure 1d), leaving only V-shaped background, we conclude that the observed gap at about 4.2 K is the superconducting gap. The superconducting gap value, Δ, can be derived using following procedure.[6,19] Polynomial functions were used to fit the backgrounds for the positive and negative bias regions and extended to the Fermi energy. After the background was removed, the spectrum was fitted using the s-wave BCS gap function with a Dynes broadening factor Γ,[20] convoluted with the Fermi function at 4.2 K. The fitted curve is plotted against the dotted data points in the left panel of Figure 1d.[21] The derived gap value is Δ = 2.3 meV. With T_c = 14 K, $2\Delta/k_B T_c$ is ~3.8, which is consistent with the value reported previously.[6]

To investigate the relationship of local surface chemistry, structure, and superconductivity, we zoom into a small area with a size of 8.4 nm × 8.4 nm (Figure 2a). In addition to the normal square lattice with bright and dark contrast, a bright spot appears at the left. There have been reports about bright spots on the Fe(Te,Se) surface, which have been attributed to local excess iron.[5,6] Song et al.[9] reported that iron ad-atoms on the FeSe surface introduce resonance states in the superconducting gap. Simultaneously taken dI/dV image (Figure 2b) at the approximate coherence peak energy (3 meV) shows contrast different from the topographic image in Figure 2a. This indicates that, in the topographic image, the apparent height difference is a real geometric effect rather than a difference in electronic
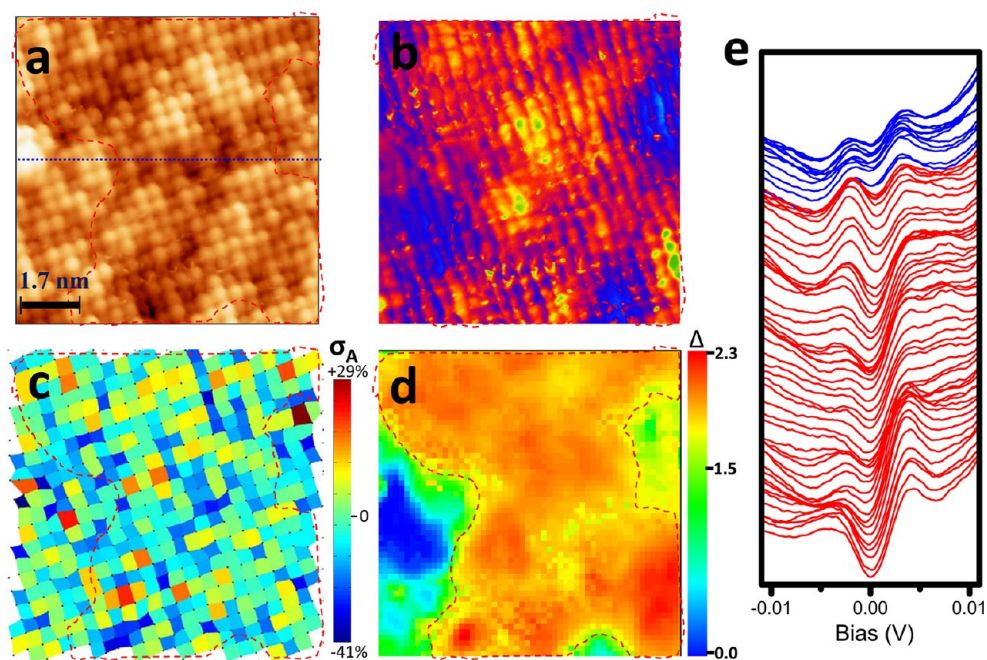
Figure 2. Comparison of an LDOS (dI/dV) map and its corresponding superconducting gap map, including the structural analysis. (a) Typical topographic image of the sample, which shows an area of 8.4 nm × 8.4 nm taken at bias of −3 mV (after bias offset of −2 mV for small biases is corrected). (b) LDOS (dI/dV) map, obtained simultaneously with topographic image at bias of −3 mV (after bias offset of −2 mV for small biases is corrected). (c) Lattice distortion mapping from local crystallographic analysis for the same location. (d) Superconducting gap map, obtained from 60 × 60 pixel local differential conductance spectral grid which was taken on the same region in (a) with a sample bias voltage of 20 mV, a tunneling current of 0.1 nA, and bias modulation amplitude of 0.3 mV$_{rms}$, showing the spatial variation of the superconducting energy gap. (e) Typical series of dI/dV spectra illustrating how the superconducting gap magnitude varies on the nanoscale, which are extracted from the same spectral survey for creating (d), along the blue dotted line shown in (a); from top to bottom, the corresponding spatial location moves to the right, away from the bright spot. The blue spectra near the bright spot show smaller gap magnitude than the spectra away from the bright spot. All spectral surveys were taken with a sample bias voltage of 20 mV, a tunneling current of 0.1 nA, and bias modulation amplitude of 0.3 mV$_{rms}$. Red dashed curves in (a−d) show the contour of the patches in the gap mapping in (d) and illustrate whether the inhomogeneity for each of the other three figures is the same as the inhomogeneity of the spatial gap.

density of states (DOS).[7] Electronic inhomogeneity exhibited in conductance mapping cannot be directly related to the inhomogeneity in surface chemistry (clustering of Te/Se). To get further insight into the detailed structure, we adapt direct local crystallographic analysis (DLCA), an approach originally developed for TEM image analysis of ferroelectric materials[22,23] and subsequently adapted for STEM[24−26] (see Materials and Methods for details). The displacement of surface apical chalcogen atoms from the unperturbed position in the lattice is identified, and a map of lattice area σ_A, which is defined in Figure 1b as the projected area onto the *ab* plane of nearest neighboring four apical chalcogen atoms, is plotted in Figure 2c. The local crystallographic inhomogeneity shown in this mapping indicates the local tetrahedral distortion within individual crystal unit cells. One important question is how superconductivity responds to this local distortion. To answer this question, it is necessary to compare the changes of interatomic distances with changes in the superconducting electronic structure inside the same unit cell.

To obtain further insight into the variability of superconductive behavior, we adopt the spectroscopic imaging approach that was originally developed for

cuprates.[27,28] A spectroscopic survey was taken on the same region in Figure 2a, which consisted of differential tunneling conductance spectra (dI/dV *versus V*) measured at grids in the given field of view. The spatial mapping of energy gap Δ ("gap maps" shown in Figure 2d) can then be derived by fitting each dI/dV spectrum with the fitting procedure described above. In the spatially resolved gap mapping, we find that the superconducting gap decreases dramatically near the bright spot, showing a significant suppression. To further confirm this, a series of dI/dV spectra across the bright spot are shown in Figure 2e, illustrating how the superconducting gap was suppressed around the bright spot. The suppression of superconductivity around the bright spot on FeTe$_{0.55}$Se$_{0.45}$ is different from the resonance states induced by iron ad-atoms on the FeSe surface.[9] While there is no conclusive evidence to determine what the extra atoms of the bright spot are, our results have clearly demonstrated that the extra atoms of the bright spot on FeTe$_{0.55}$Se$_{0.45}$ suppress the superconductivity around the bright spot.

In the rest of the region, we find that the superconducting gap is rather uniform, varying slightly with spatial locations in the range of 1.5 to 2.3 meV. The gap
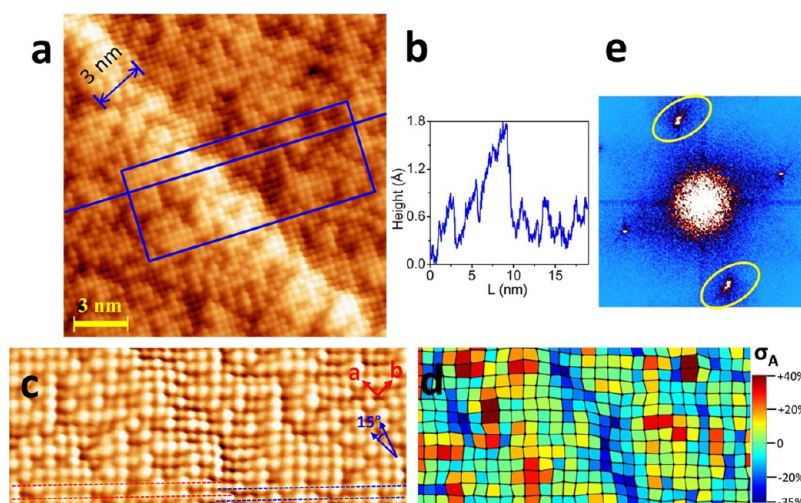
Figure 3. Distortion domain of Fe(Se,Te). (a) Topographic image showing a distortion boundary. Scan size is 18 nm × 18 nm. The image was taken at the bias of 50 mV with 100 pA tunneling current. (b) Typical height profile across the defect. (c) Zoomed-in image of the defect corresponding to the boxed area in (a), showing lattice shifting on the distortion domain. The image has been processed (smoothed and flattened) to better illustrate the lattice shifting. (d) Lattice distortion mapping from local crystallographic analysis for the defect. (e) FFT for the image in (a).

mapping exhibits small patches with the gap value of 2.2 meV, and the size of patches is in the scale of 2−4 nm, close to the reported superconducting coherence length in FeSe.[29] The spatial gap variations have no one-to-one correspondence to the local crystallographic map. In fact, the gap energy varies on the 2−4 nm length scale in our case, whereas the displacement changes at every other Se(Te) atom (0.38 nm length scale) in Figure 2c. This demonstrates that the individual local lattice distortion due to chemical inhomogeneity, as reflected in variations in local lattice area or height of surface chalcogen atoms, does not modulate correspondingly the superconducting gap. These observations provide the context for studies of superconductive behavior at local defects reported below.

To investigate how the geometry of an $Fe(Se, Te)_4$ tetrahedron affects superconductivity locally, it would be essential to find a local region in which the crystal structure is continuously perturbed with a spatial size slightly larger than or comparable to the superconducting coherence length of the material, similar to what is suggested for investigating the local structure dependence of superconductivity in cuprates by Slezak et al.[1] Upon examining large areas of the $FeTe_{0.55}Se_{0.45}$ surface, we observed the boundary-like region, shown in Figure 3a (refer to Supporting Information for large-scale image (Figure S1)). These defects are observed in multiple locations on this surface. Such defect is typically more than 100 nm long (beyond the area shown in the figure), having an apparent height of the feature about 1.0−1.2 Å. More importantly, the width of the defect is about 2−4 nm, comparable to the superconducting coherence length for FeSe. Furthermore, the boundary-like region can be atomically resolved, allowing for identification of the defect

type. We note that a recent report has shown that superconductivity is suppressed in FeSe by twin boundaries,[29] which form in the orthorhombic ferroelastic phase of FeSe. Upon cooling, FeSe changes from tetragonal to orthorhombic structure, giving rise to twin boundaries,[29] while optimally doped $FeTe_{0.55}Se_{0.45}$ remains tetragonal. In Figure 3a, we do not observe twin domains in the areas at two sides of the boundary-like region. Thus, the boundary-like defect we observed in $FeTe_{0.55}Se_{0.45}$ is not the twin boundary, but there are distortions as we will demonstrate below.

In order to study the defect structure in more detail, we focus on an image taken at the boundary region (marked by blue rectangle in Figure 3a). A series of parallel dashed lines are used to guide the eyes (Figure 3c). The lattices on the left and right sides of boundary shift by half a unit cell over about nine unit cell transition zones. Here, we refer to the region with anomalous structure as the distortion domain. In this region, the lattice develops the half unit cell shift by a continuous distortion along one of the nearest-neighbor chalcogen atom directions in the topmost layer. The boundary is oriented along a 15° angle with respect to the Fe−Fe bond directions. Here, a and b correspond to the two Fe−Fe bonding directions, as defined in Figure 3c. The detailed structure of this boundary is analyzed by applying direct crystallographic analysis on the atomic resolution STM image. The deviations from the unperturbed lattice for atoms in the distortion domain are plotted in Figure 3d as well as the spatial variations of the lattice area, σ_A, defined previously. Strong lattice distortion on the boundary is observed, and the lattice area is greatly compressed by ≈35% in the boundary region. Such compressed lattice area can be interpreted as following. In order to adopt the antiphase lattice shifting, the distortion boundary not only induces the
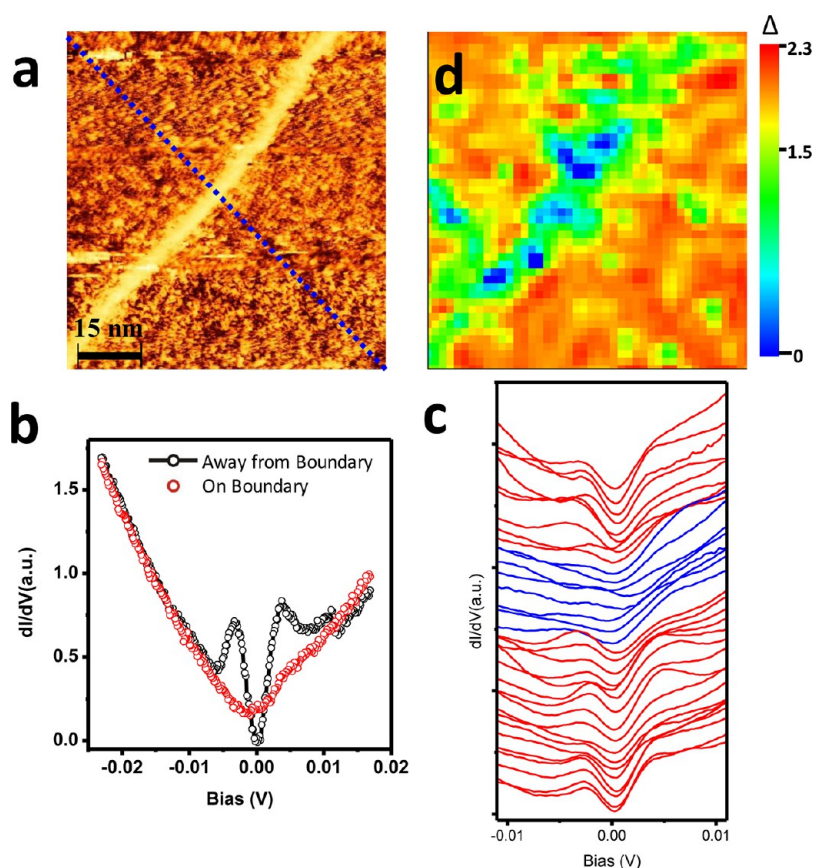
Figure 4. STM characterization of Fe(Se,Te). (a) Topographic image showing an area of 75 nm (width) × 79 nm (length) taken at a bias of 20 mV. (b) Two spectra measured at two randomly selected locations of the boundary region and away from the boundary region. (c) Series of dI/dV spectra across the structural distortion line. These unprocessed spectra were generated from a single spectral survey which was taken on the same region in (a), along the blue dotted line shown in (a). From top to bottom, the corresponding spatial location moves from upper left to lower right along the blue dotted line in (a). The red spectra are away from the distortion domain; the blue spectra are at the distortion domain showing suppression of superconductivity gap. (d) High-resolution gap map revealing a stripe embedded in the superconducting background. The color scale spans the range of 0−2.3 meV. This gap map corresponds to the same region in (a) and is calculated from same spectral surveys for (b). The interconnected red, orange, and yellow regions are high Δ regions. Embedded stripe domain is green and blue low-Δ regions.

lattice contraction (Figure 3d) but also leads to a significant lattice twisting, which can also be clearly observed as the elongation of spots in reciprocal space highlighted with yellow ellipse in the Fourier image of Figure 3a (Figure 3e). Here, such local distortion may be induced by the segregation of chalcogen atoms in a 1D-like structure, with an associated change in the lattice parameter and a "kink" in the lattice (which would be forbidden in the "patches").

The formation of the defect in Figure 3a is accompanied by an increase in the chalcogen heights, which can be clearly observed from the height profile in Figure 3b. The height of surface chalcogen atoms h_{anion} at the boundary region is about 1.0 Å higher than the average surface plane. Considering that the average anion height of apical chalcogen atoms is about 1.60 Å (based on $h_{anion-Te}$ = 1.72 Å and $h_{anion-Se}$ = 1.48 Å in FeSe$_{0.44}$Te$_{0.56}$),[30] apical chalcogen atoms at the boundary are up to 2.6 Å away from the Fe–Fe plane. In fact, the tetrahedral geometry in iron-based superconductors may be a key factor for superconductivity, where

the tetrahedral angle and h_{anion} are both considered to be important factors.[29,31−35] In some previous studies, it has been shown that the tetrahedral angle in iron chalcogenides has no significant effect on T_c.[32,36] It is demonstrated that h_{anion} may be correlated to the value of T_c in the iron-based superconductors, reaching a maximum T_c for $h_{anion} \sim$ 1.38 Å.[34,35] With our material having aforementioned average $h_{anion} \sim$ 1.60 Å,[30] a further increase of h_{anion} is expected to lead to suppression of T_c at our distortion boundary, similar to the reported case for FeSe.[29]

We further explore the behavior of the superconductive order parameter in the distortion domain as compared to the pristine surface area. The dI/dV spectrum on the boundary region shows only a V-shaped background, without any superconducting gap feature (Figure 4b). We show in Figure 4c the unprocessed dI/dV spectra measured along the blue dotted line in Figure 4a to illustrate how the electronic phenomena behave in the raw data. The spectral evolution across the distortion boundary is easily seen.

Figure 4d shows the spatial evolution of the gap $\Delta(r)$. This mapping demonstrates a stripe running diagonally, in spatial agreement with the location of the distortion boundary in Figure 4a. The stripe is characterized with a low value of Δ. From the domain edge to the domain center, the superconducting gap value $\Delta(r)$ drops toward zero in a few nanometer scale. In previous studies, FeTe[37] has the so-called "double stripe" $(\pi, 0)$ antiferromagnetism (AFM) ordering vector,[38,39] while all other iron-based superconductors exhibit the "single stripe" (π, π) ordering vector.[34] Adding Se in $FeSe_xTe_{1-x}$ is reported to suppress $(\pi, 0)$ spin fluctuations and enhance (π, π) fluctuations, leading to superconductivity.[36,40] From undoped FeSe to FeTe, the anion height h_{anion} increases accordingly from 1.45 to 1.81 Å.[36] Previous theoretical studies have also shown that the anion height h_{anion} plays an important role in the magnetic ordering and thus affects superconductivity in Fe(Te, Se); the double stripe $(\pi, 0)$ magnetic ordering in FeTe with optimized Te height changes to the single stripe (π, π) ordering when the height of Te is reduced below a critical value by doping Se.[36]

CONCLUSION

In summary, we explore the interplay between local structure, chemical composition, and superconductivity in an $FeTe_{0.55}Se_{0.45}$ crystal using a combination of local crystallographic analysis and dI/dV mapping. We demonstrate that local segregation of chalcogens leads to minor structural changes in bond length and angles in $Fe(Se,Te)_4$ tetrahedra but does not affect dramatically the local superconductive order parameter. The formation of defects leads to local changes of crystallographic symmetry and a kink-like lattice structure, allowing for a larger scale relaxation of lattice parameters. Such distortion defects were observed to induce the local suppression of superconductivity. These studies thus differentiate the role of chemical and structural inhomogeneity on superconductive behavior and illustrate that chemical segregation can affect a superconducting state upon structural relaxation. Beyond the Fe-based superconductor, we provide a new paradigm for atomic-level probing of local functionalities and link between structure and property and provide the impetus for the development of the next generation of high-resolution microscopic platforms.

MATERIALS AND METHODS

Synthesis of the $FeSe_{1-x}Te_x$ Sample. Single crystals of $FeTe_{0.55}Se_{0.45}$ are grown by a modified Bridgman method. A mixture of millimeter-sized Fe pieces (99.99%) and Se and Te shot (>99.999%) with the stoichiometry of $FeTe_{0.55}Se_{0.45}$ are loaded into a pointed silica ampule and sealed under vacuum. This ampule is vacuum-sealed inside another silica ampule in case the inner ampule cracks on cooling. The ampules are then heated to 1100 °C over 12 h, held at 1100 °C for 30 h (with some mechanical stirring of the liquid at temperature), cooled to 400 °C at 6 °C/h, held at 400 °C for 4 days, and then furnace-cooled to room temperature over 12 h. The crystals selected for the STM experiments are from the bottom of the crystalline boule and have chemical compositions close to the nominal value, $FeTe_{0.55}Se_{0.45}$, as is found by the energy-dispersive X-ray spectroscopy. The chemical composition is accurate to within 2% for each of the elements. The superconducting properties of the crystals are measured both magnetically and resistively. The zero-field-cooled magnetic signal at 20 Oe shows 100% diamagnetic screening and a transition width (10−90%) of 2 K, with an onset temperature near 15 K. The superconducting transition temperature (midpoint) for both resistivity and magnetic measurements is near 14 K.

STM Measurements. A laboratory-built low-temperature scanning tunneling microscope (STM) was used for the imaging and spectroscopic measurements. The sample was cleaved at room temperature in an ultrahigh vacuum (UHV) to expose a clean surface and then loaded into the STM head for investigation at about 77 and 4.2 K. We obtained topographic images in constant-current mode and the tunneling spectra dI/dV using a lock-in technique to measure differential conductance. The WSxM software has been used to process and analyze STM data.[41]

Local Crystallographic Analysis. In this method, the locations of all atoms in the image are indexed to a best fit ideal square lattice, assigning to each atom a set of (i,j) indexes allowing the spatial (x,y) deviation of each atom from the ideal lattice position to be determined. The best fit lattice was determined by a least-squares minimization of the difference between a topographic image (with max height normalized to 1 and average height set to 0) and a lattice composed of hemispherical atoms on a grid described by 6 parameters: atomic spacings along the x direction and y direction, x and y displacement of the grid from the image center, rotation about the image center, and skew (displacement of atoms in the x direction proportional to atoms at y position). Lattice skew was included to account for drift during imaging. The height and position of each atom in an image was determined from the fit of each atom individually using an automated process. Initial estimates of atom positions used during fitting were determined by thresholding the topographic image and finding the centroid of the remaining isolated regions of pixels.

Conflict of Interest: The authors declare no competing financial interest.

Supporting Information Available: Supplementary figures. This material is available free of charge *via* the Internet at http://pubs.acs.org.

REFERENCES AND NOTES

1. Slezak, J. A.; Lee, J.; Wang, M.; McElroy, K.; Fujita, K.; Andersen, B. M.; Hirschfeld, P. J.; Eisaki, H.; Uchida, S.; Davis, J. C. Imaging the Impact on Cuprate Superconductivity of Varying the Interatomic Distances within Individual Crystal Unit Cells. *Proc. Natl. Acad. Sci. U.S.A.* **2008**, *105*, 3203–3208.

2. Louca, D.; Horigane, K.; Llobet, A.; Arita, R.; Ji, S.; Katayama, N.; Konbu, S.; Nakamura, K.; Koo, T.-Y.; Tong, P.; *et al.* Local Atomic Structure of Superconducting $FeSe_{1-x}Te_x$. *Phys. Rev. B* **2010**, *81*, 134524.

3. Zeljkovic, I.; Xu, Z.; Wen, J.; Gu, G.; Markiewicz, R. S.; Hoffman, J. E. Imaging the Impact of Single Oxygen Atoms on Superconducting $Bi_{2+y}Sr_{2-y}CaCu_2O_{8+x}$. *Science* **2012**, *337*, 320–323.

4. Hoffman, J. E. Spectroscopic Scanning Tunneling Microscopy Insights into Fe-Based Superconductors. *Rep. Prog. Phys.* **2011**, *74*, 124513.

5. Massee, F.; de Jong, S.; Huang, Y.; Kaas, J.; van Heumen, E.; Goedkoop, J. B.; Golden, M. S. Cleavage Surfaces of the $BaFe_{2-x}Co_xAs_2$ and $Fe_ySe_{1-x}Te_x$ Superconductors: A Combined STM Plus LEED Study. *Phys. Rev. B* **2009**, *80*, 140507.

6. Kato, T.; Mizuguchi, Y.; Nakamura, H.; Machida, T.; Sakata, H.; Takano, Y. Local Density of States and Superconducting Gap in the Iron Chalcogenide Superconductor $Fe_{1+\delta}Se_{1-x}Te_x$ Observed by Scanning Tunneling Spectroscopy. *Phys. Rev. B* **2009**, *80*, 180507.

7. He, X.; Li, G.; Zhang, J.; Karki, A. B.; Jin, R.; Sales, B. C.; Sefat, A. S.; McGuire, M. A.; Mandrus, D.; Plummer, E. W. Nanoscale Chemical Phase Separation in $FeTe_{0.55}Se_{0.45}$ as Seen *via* Scanning Tunneling Spectroscopy. *Phys. Rev. B* **2011**, *83*, 220502.

8. Hanaguri, T.; Niitaka, S.; Kuroki, K.; Takagi, H. Unconventional s-Wave Superconductivity in Fe(Se,Te). *Science* **2010**, *328*, 474–476.

9. Song, C.-L.; Wang, Y.-L.; Cheng, P.; Jiang, Y.-P.; Li, W.; Zhang, T.; Li, Z.; He, K.; Wang, L.; Jia, J.-F.; *et al.* Direct Observation of Nodes and Twofold Symmetry in FeSe Superconductor. *Science* **2011**, *332*, 1410–1413.

10. Qazilbash, M. M.; Brehm, M.; Chae, B.-G.; Ho, P.-C.; Andreev, G. O.; Kim, B.-J.; Yun, S. J.; Balatsky, A. V.; Maple, M. B.; Keilmann, F.; *et al.* Mott Transition in VO_2 Revealed by Infrared Spectroscopy and Nano-imaging. *Science* **2007**, *318*, 1750–1753.

11. Tselev, A.; Stelcov, E.; Jones, K.; Proksch, R.; Kolmakov, A.; Kalinin, S. Scanning Microwave Microscopy Studies of Metal-Insulator Transition at Ferroelastic Domain Walls in VO_2. *Microsc. Microanal.* **2010**, *16*, 460–461.

12. Tselev, A.; Budai, J. D.; Strelcov, E.; Tischler, J. Z.; Kolmakov, A.; Kalinin, S. V. Electromechanical Actuation and Current-Induced Metastable States in Suspended Single-Crystalline VO_2 Nanoplatelets. *Nano Lett.* **2011**, *11*, 3065–3073.

13. Cao, J.; Fan, W.; Zheng, H.; Wu, J. Thermoelectric Effect Across the Metal-Insulator Domain Walls in VO_2 Microbeams. *Nano Lett.* **2009**, *9*, 4001–4006.

14. Jones, A. C.; Berweger, S.; Wei, J.; Cobden, D.; Raschke, M. B. Nano-optical Investigations of the Metal-Insulator Phase Behavior of Individual VO_2 Microcrystals. *Nano Lett.* **2010**, *10*, 1574–1581.

15. Jesse, S.; Rodriguez, B. J.; Choudhury, S.; Baddorf, A. P.; Vrejoiu, I.; Hesse, D.; Alexe, M.; Eliseev, E. A.; Morozovska, A. N.; Zhang, J.; *et al.* Direct Imaging of the Spatial and Energy Distribution of Nucleation Centres in Ferroelectric Materials. *Nat. Mater.* **2008**, *7*, 209–215.

16. Balke, N.; Winchester, B.; Ren, W.; Chu, Y. H.; Morozovska, A. N.; Eliseev, E. A.; Huijben, M.; Vasudevan, R. K.; Maksymovych, P.; Britson, J.; *et al.* Enhanced Electric Conductivity at Ferroelectric Vortex Cores in $BiFeO_3$. *Nat. Phys.* **2012**, *8*, 81–88.

17. Maksymovych, P.; Jesse, S.; Yu, P.; Ramesh, R.; Baddorf, A. P.; Kalinin, S. V. Polarization Control of Electron Tunneling into Ferroelectric Surfaces. *Science* **2009**, *324*, 1421–1425.

18. Sales, B. C.; Sefat, A. S.; McGuire, M. A.; Jin, R. Y.; Mandrus, D.; Mozharivskyj, Y. Bulk Superconductivity at 14 K in Single Crystals of $Fe_{1+y}Te_xSe_{1-x}$. *Phys. Rev. B* **2009**, *79*, 094521.

19. Jin, R.; Pan, M. H.; He, X. B.; Li, G.; Li, D.; Peng, R.; Thompson, J. R.; Sales, B. C.; Sefat, A. S.; McGuire, M. A.; *et al.* Electronic, Magnetic and Optical Properties of Two Fe-Based Superconductors and Related Parent Compounds. *Supercond. Sci. Technol.* **2010**, *23*, 054005.

20. Dynes, R. C.; Narayanamurti, V.; Garno, J. P. Direct Measurement of Quasiparticle-Lifetime Broadening in a Strong-Coupled Superconductor. *Phys. Rev. Lett.* **1978**, *41*, 1509–1512.

21. Using the position of two coherence peaks is an easy way to determine the gap value. However, this is only applicable when the measuring temperature is far below T_c. In that case, the coherence peaks are sharp and well-defined, for example, measuring high T_c cuprates at 4 K. In our case, the measuring temperature of ~4.2 K is close to T_c and the thermal broadening of the coherence peaks used to make such method not applicable.

22. Jia, C.-L.; Nagarajan, V.; He, J.-Q.; Houben, L.; Zhao, T.; Ramesh, R.; Urban, K.; Waser, R. Unit-Cell Scale Mapping of Ferroelectricity and Tetragonality in Epitaxial Ultrathin Ferroelectric Films. *Nat. Mater.* **2007**, *6*, 64–69.

23. Jia, C.-L.; Mi, S.-B.; Urban, K.; Vrejoiu, I.; Alexe, M.; Hesse, D. Atomic-Scale Study of Electric Dipoles near Charged and Uncharged Domain Walls in Ferroelectric Films. *Nat. Mater.* **2008**, *7*, 57–61.

24. Borisevich, A. Y.; Chang, H. J.; Huijben, M.; Oxley, M. P.; Okamoto, S.; Niranjan, M. K.; Burton, J. D.; Tsymbal, E. Y.; Chu, Y. H.; Yu, P.; *et al.* Suppression of Octahedral Tilts and Associated Changes in Electronic Properties at Epitaxial Oxide Heterostructure Interfaces. *Phys. Rev. Lett.* **2010**, *105*, 087204.

25. Nelson, C. T.; Winchester, B.; Zhang, Y.; Kim, S.-J.; Melville, A.; Adamo, C.; Folkman, C. M.; Baek, S.-H.; Eom, C.-B.; Schlom, D. G.; *et al.* Spontaneous Vortex Nanodomain Arrays at Ferroelectric Heterointerfaces. *Nano Lett.* **2011**, *11*, 828–834.

26. Chisholm, M. F.; Luo, W.; Oxley, M. P.; Pantelides, S. T.; Lee, H. N. Atomic-Scale Compensation Phenomena at Polar Interfaces. *Phys. Rev. Lett.* **2010**, *105*, 197602.

27. Lang, K.; Madhavan, V.; Hoffman, J.; Hudson, E.; Eisaki, H.; Uchida, S.; Davis, J. Imaging the Granular Structure of High-T_c Superconductivity in Underdoped $Bi_2Sr_2CaCu_2O_{8+\delta}$. *Nature* **2002**, *415*, 412–416.

28. Pan, S. H.; O'Neal, J. P.; Badzey, R. L.; Chamon, C.; Ding, H.; Engelbrecht, J. R.; Wang, Z.; Eisaki, H.; Uchida, S.; Guptak, A. K.; *et al.* Microscopic Electronic Inhomogeneity in the high-T_c Superconductor $Bi_2Sr_2CaCu_2O_{8+x}$. *Nature* **2001**, *413*, 282–285.

29. Song, C.-L.; Wang, Y.-L.; Jiang, Y.-P.; Wang, L.; He, K.; Chen, X.; Hoffman, J. E.; Ma, X.-C.; Xue, Q.-K. Suppression of Superconductivity by Twin Boundaries in FeSe. *Phys. Rev. Lett.* **2012**, *109*, 137004.

30. Tegel, M.; Löhnert, C.; Johrendt, D. The Crystal Structure of $FeSe_{0.44}Te_{0.56}$. *Solid State Commun.* **2010**, *150*, 383–385.

31. Johnston, D. C. The Puzzle of High Temperature Superconductivity in Layered Iron Pnictides and Chalcogenides. *Adv. Phys.* **2010**, *59*, 803–1061.

32. Huang, S. X.; Chien, C. L.; Thampy, V.; Broholm, C. Control of Tetrahedral Coordination and Superconductivity in $FeSe_{0.5}Te_{0.5}$ Thin Films. *Phys. Rev. Lett.* **2010**, *104*, 217002.

33. Horigane, K.; Hiraka, H.; Ohoyama, K. Relationship between Structure and Superconductivity in $FeSe_{1-x}Te_x$. *J. Phys. Soc. Jpn.* **2009**, *78*, 074718.

34. Okabe, H.; Takeshita, N.; Horigane, K.; Muranaka, T.; Akimitsu, J. Pressure-Induced High-T_c Superconducting Phase in FeSe: Correlation between Anion Height and T_c. *Phys. Rev. B* **2010**, *81*, 205119.

35. Mizuguchi, Y.; Hara, Y.; Deguchi, K.; Tsuda, S.; Yamaguchi, T.; Takeda, K.; Kotegawa, H.; Tou, H.; Takano, Y. Anion Height Dependence of T_c for the Fe-Based Superconductor. *Supercond. Sci. Technol.* **2010**, *23*, 054013.

36. Moon, C.-Y.; Choi, H. J. Chalcogen-Height Dependent Magnetic Interactions and Magnetic Order Switching in $FeSe_xTe_{1-x}$. *Phys. Rev. Lett.* **2010**, *104*, 057003.

37. FeTe does not form. The closest to FeTe is about $Fe_{1.07}Te$, with the 7% extra iron located roughly at the same height as either Te or Se. This extra iron donates electrons and moves the Fermi energy in a rigid band picture. According to Singh's calculation, this excess iron also is magnetic, *i.e.*, has a well-defined magnetic moment. A local moment like this is expected to break pairs and suppress superconductivity. Extra magnetism added by the 7% iron is expected to be enough to polarize the other iron d band and induce magnetism.

38. Li, S.; de la Cruz, C.; Huang, Q.; Chen, Y.; Lynn, J. W.; Hu, J.; Huang, Y.-L.; Hsu, F.-C.; Yeh, K.-W.; Wu, M.-K.; *et al.* First-Order Magnetic and Structural Phase Transitions in $Fe_{1+y}Se_xTe_{1-x}$. *Phys. Rev. B* **2009**, *79*, 054503.

39. Ma, F.; Ji, W.; Hu, J.; Lu, Z.-Y.; Xiang, T. First-Principles Calculations of the Electronic Structure of Tetragonal α-FeTe and α-FeSe Crystals: Evidence for a Bicollinear Antiferromagnetic Order. *Phys. Rev. Lett.* **2009**, *102*, 177003.

40. Qiu, Y.; Bao, W.; Zhao, Y.; Broholm, C.; Stanev, V.; Tesanovic, Z.; Gasparovic, Y. C.; Chang, S.; Hu, J.; Qian, B.; *et al.* Spin Gap and Resonance at the Nesting Wave Vector in Superconducting $FeSe_{0.4}Te_{0.6}$. *Phys. Rev. Lett.* **2009**, *103*, 067008.

41. Horcas, I.; Fernández, R.; Gómez-Rodríguez, J. M.; Colchero, J.; Gómez-Herrero, J.; Baro, A. M. WSXM: A Software for Scanning Probe Microscopy and a Tool for Nanotechnology. *Rev. Sci. Instrum.* **2007**, *78*, 013705.